

## Article

# Microstructure Evolution and Wear Resistance of the Eutectic High-Entropy Alloy $\text{Al}_{0.3}\text{CoCrFeNiNb}_{0.5}$ Produced by Laser Metal Deposition

Bianca Preuß <sup>1,\*</sup> , Thomas Lindner <sup>1</sup> , Thomas Uhlig <sup>1</sup> , Jorge Eduardo Tapia Cabrera <sup>1</sup>, Holger Schwarz <sup>2</sup> , Guntram Wagner <sup>1</sup> , Thomas Seyller <sup>2,3</sup>  and Thomas Lampke <sup>1</sup> 

<sup>1</sup> Institute of Materials Science and Engineering, Faculty of Mechanical Engineering, Chemnitz University of Technology, 09107 Chemnitz, Germany

<sup>2</sup> Institute of Physics, Faculty of Natural Sciences, Chemnitz University of Technology, 09126 Chemnitz, Germany

<sup>3</sup> Center for Materials, Architectures and Integration of Nanomembranes (MAIN), Chemnitz University of Technology, 09107 Chemnitz, Germany

\* Correspondence: bianca.preuss@mb.tu-chemnitz.de; Tel.: +49-(37)-153136611

**Abstract:** Eutectic high-entropy alloys (EHEAs) are characterized by a fine lamellar microstructure. This allows for homogeneous functional surface properties. Furthermore, the risk of coarse precipitate formation during coating processes from the liquid state is avoided. However, the influence of the size and the texture of the local microstructure domain on functional properties is still unknown. The present work is devoted to the microstructural evolution of the EHEA  $\text{Al}_{0.3}\text{CoCrFeNiNb}_{0.5}$ . Inert gas atomized powder was processed by laser metal deposition (LMD) and spark plasma sintering (SPS). Both specimens were heat treated near their liquidus temperatures. The different production routes have a decisive influence on the orientation of the lamellar structure. The SPS bulk material has a statistically distributed orientation of the lamellae defined by the microstructure of the powder. However, the remelting of the powder during the LMD process causes a directional vertical solidification of the lamellar structure. Based on these differences, positive effects on their functional properties were detected for directionally solidified LMD coatings. As a result of the heat treatment, the influence of the lamellar orientation on their tribological properties is reduced, whereas the influence of the lamellar size on their property profile can be derived.

**Keywords:** high-entropy alloy; HEA; spark plasma sintering; SPS; laser metal deposition; LMD; eutectic high-entropy alloy; EHEA; heat treatment



**Citation:** Preuß, B.; Lindner, T.; Uhlig, T.; Tapia Cabrera, J.E.; Schwarz, H.; Wagner, G.; Seyller, T.; Lampke, T. Microstructure Evolution and Wear Resistance of the Eutectic High-Entropy Alloy  $\text{Al}_{0.3}\text{CoCrFeNiNb}_{0.5}$  Produced by Laser Metal Deposition. *Coatings* **2023**, *13*, 585. <https://doi.org/10.3390/coatings13030585>

Academic Editor: Frederic Sanchette

Received: 10 February 2023

Revised: 3 March 2023

Accepted: 6 March 2023

Published: 8 March 2023



**Copyright:** © 2023 by the authors. Licensee MDPI, Basel, Switzerland. This article is an open access article distributed under the terms and conditions of the Creative Commons Attribution (CC BY) license (<https://creativecommons.org/licenses/by/4.0/>).

## 1. Introduction

High-entropy alloys (HEAs) consist of at least five alloying elements with an atomic content between 5% and 35% [1]. Several studies have already demonstrated the potential of these alloys, particularly in the field of surface protection [2]. Furthermore, eutectic high-entropy alloys (EHEAs) represent a promising approach for coating technologies such as laser metal deposition (LMD) [3]. The risk of coarse segregations during liquid state coating processes is avoided by a fine lamellar microstructure. Although this allows for homogeneous surface properties, the size, shape and texture of the microscopically heterogeneous eutectic structure can influence the property profile. LMD allows for crucial cooling conditions to be controlled by processing parameters. However, predictable and consistent coating properties depend not least on the integrity of the microstructure. Therefore, the effects of thermal exposure also need to be considered. A property-determining influence from the heat treatment of EHEAs has already been confirmed in several studies [4–8]. From these studies, an influence from the alloy composition and the primary structure can be derived. So far, microstructure characteristics and their stability have not been investigated for EHEA coating systems.

Vacuum arc melting is a well-established production route for exploring new alloy compositions in the field of HEAs and EHEAs [4–7]. Lu et al. [8] investigated for the first time the EHEA AlCoCrFeNi<sub>2.1</sub>. This alloy system is characterized by high room temperature strength and ductility [8]. Subsequently, further EHEAs with refractory metal additives were developed and investigated in the as-cast state [9–12]. In a previous study, a fine lamellar structure was detected for the EHEA Al<sub>0.3</sub>CoCrFeNiNb<sub>0.5</sub> in its as-cast state. Furthermore, a high hardness and wear resistance was determined [13]. Due to the variation in cooling conditions during solidification between the surface and the center of the casting, different microstructural domains are formed. Casting defects such as elemental segregations, cracks and pores as well as the suppression of equilibrium phases influence the property profile [1]. Furthermore, elongated columnar grain structures are primarily formed [14,15]. In addition to melt metallurgical production routes such as vacuum arc melting, powder metallurgical approaches are also used to produce bulk materials. In comparison with various sintering processes, the spark plasma sintering (SPS) process in particular offers an efficient and cost-effective option for producing fine crystalline bulk materials [16]. A wide variety of HEAs has been produced by SPS processes [4,17–19]. Large regular grains were detected in SPS Al<sub>x</sub>CoCrCuFeNi bulk material while a dendritic structure was observed in the arc-melted samples [20]. The same difference between the two processing routines was found for the HEA Al<sub>x</sub>FeNiCrCo [21]. Investigations of the SPS EHEA AlCoCrFeNi<sub>2.1</sub> showed a dependency of the microstructure on the sintering temperature. The hardness and wear resistance were improved by a pronounced lamellar structure [22]. Compared to SPS, higher cooling rates of 10<sup>3</sup> and 10<sup>4</sup> K/s [23] for the LMD process led to a fine lamellar structure [24]. LMD is assigned to the route from the liquid state. The bond between the coating and the substrate is characterized by high adhesion [1,24]. Various HEAs have been successfully prepared by LMD [25,26]. Due to the direct change to the liquid state, EHEAs are particularly well suited for coating preparation by LMD [27]. Therefore, casting defects and segregation can be effectively reduced [28]. Huang et al. [29] detected a fine and regularly distributed lamellar structure in the LMD AlCoCrFeNi<sub>2.1</sub>. Hence, its properties were improved compared to the casting [29]. If HEAs or EHEAs are exposed to heat treatment, their microstructure domain and mechanical properties can vary [30–32]. Moravcik et al. [4] observed a decrease in the hardness of the sintered HEA AlCoCrFeNiTi<sub>0.5</sub> due to a heat treatment at 1100 °C and 1250 °C for 2 h. Sriharitha et al. [20] detected no significant decrease in the hardness of the SPS HEAs Al<sub>0.45</sub>CoCrCuFeNi and AlCoCrCuFeNi after annealing at 600 °C for 10 h. John et al. [32] recorded a phase transformation of the SPS EHEA AlCoCrFeNi<sub>2.1</sub>. The B2 phase changed to a disordered BCC phase after heat treatment at 1200 °C for 1 h and 5 h.

In the present study, the powder feedstock of the EHEA Al<sub>0.3</sub>CoCrFeNiNb<sub>0.5</sub> was used to produce the bulk materials by SPS and coatings via LMD. Based on the different process conditions during SPS and LMD and heat treatment, the size and the texture of the local microstructure domain were investigated. The influence of the microstructure's evolution on the tribological properties was determined. Hence, an analysis of the relation between production routes, microstructure and the property profile can expand upon the understanding of EHEAs. Therefore, suitable application areas can be specified and derived.

## 2. Materials and Methods

In the current work, the EHEA Al<sub>0.3</sub>CoCrFeNiNb<sub>0.5</sub> was processed through the powder metallurgical processing route of SPS. This technology was applied to produce bulk materials, whereas coatings were manufactured by the melt metallurgical LMD process. Inert gas atomized powder (Nanoval GmbH & Co. KG, Berlin, Germany) was used as feedstock. The feedstock was characterized in detail in a previous study [13]. An SPS KCE FCT-HP D 25-SI (FCT Systeme GmbH, Frankenblick, Germany) was utilized to compact the feedstock powder to bulk materials with a height of 10 mm and a diameter of 40 mm. Graphite tools consisting of two graphite punches, one graphite die and two graphite cones

were needed for the SPS route. Graphite foils with a thickness of 0.3 mm were inserted between the feedstock and the punches as well as the die. Reactions with the atmosphere were prevented by flushing the recipient with argon and evacuating it twice (<2 mbar). The consolidation was carried out under a pressure of 50 MPa, at a temperature of 1050 °C and a holding time of 10 min. By a water cooling system at the punches, the cooling was carried out at a cooling rate of approx. 150 K/min down to 300 °C. The coatings were applied using an LMD consisting of a TRUMPF BEO D70 Optic with a prototype TRUMPF 7-ray nozzle and a TRUMPF TruDisk 6001 laser source. The substrate was a round blank of EN1.4301 with a thickness of 6 mm and a diameter of 100 mm. The focal point was set 1.5 mm above the substrate surface. The spot width was approx. 2 mm. A plate feeder was used to continuously feed the powder during the deposition process. The feed rate resulted from the path velocity and the trace offset. The processing was controlled by the axial rotation of a conventional industrial robot. The processing parameters are shown in Table 1.

**Table 1.** Laser metal deposition process parameters for  $\text{Al}_{0.3}\text{CoCrFeNiNb}_{0.5}$ .

| Power (W) | Path Velocity ( $\text{m}\cdot\text{s}^{-1}$ ) | Trace Offset (mm) | Feeding Rate ( $\text{g}\cdot\text{min}^{-1}$ ) | Ar Gas Flow Rate ( $\text{L}\cdot\text{min}^{-1}$ ) | Layer Thickness (mm) |
|-----------|--|-------------------|---|---|----------------------|
| 4000      | 0.5  | 0.3               | 31.0  | 12.0  | approx. 0.5          |

The bulk material and the coating were heat-treated in a vacuum furnace (Torvac 12 Mark IV) at 1100 °C, close to the liquidus temperature. The liquidus temperature was determined by DSC measurements in a previous study [13]. The heat treatment was carried out at a pressure of  $\leq 10^{-2}$  Pa for 12 h at 1100 °C. The applied heating rate was 10 K/min. Cross sections of the SPS bulk material and LMD coating were prepared for analysis using the scanning electron microscope (SEM) LEO 1455VP (Zeiss, Jena, Germany) equipped with a backscattered electron detector (BSD). The accelerating voltage was 25 kV. The integrated energy-dispersive X-ray spectroscopy (EDS) system EDS GENESIS (EDAX, Mahwah, NJ, USA) was used to determine the chemical composition. Phase investigation of the SPS bulk material and LMD coating was realized by X-ray diffraction (XRD) analysis using a Rigaku SmartLab 9 kW instrument equipped with a HyPix-3000 detector (Rigaku Corporation, Tokyo, Japan). Using  $\text{Cu-K}\alpha$  radiation (0.15406 nm), a diffraction angle ( $2\theta$ ) range between 30° and 120° was investigated. The coating thickness was determined at 20 distributed points using the optical microscope GX51 (Olympus, Shinjuku, Japan) equipped with an SC50 camera (Olympus, Shinjuku, Japan). The porosity of the bulk material and coatings was evaluated by an image analysis method with the software ImageJ. The microhardness (Vickers hardness HV0.5) was detected by the Wilson Tukon 1102 device (Buehler, Uzwil, Switzerland) on the cross sections, using a load of 4.903 N applied for five seconds. The average value was calculated from ten individual Vickers indentations for each state. Wear tests were carried out under different tribological conditions to determine the influence of the production route and the heat treatment. The wear behavior of the bulk materials and the coatings was analyzed under sliding, oscillating and abrasive wear conditions. All measurements were carried out at room temperature. The wear test parameters are shown in Table 2. Ball-on-disk testing via the Tetra Basalt Tester (Tetra, Ilmenau, Germany) was used to determine the sliding wear behavior. The scratch test was realized by the CSM Revetest-RST instrument (CSM Instruments SA, Peseux, Switzerland). For investigating the oscillating wear behavior, the Wazau SVT 40 device (Wazau, Berlin, Germany) was utilized. ASTM G 99, ASTM G 171 and ASTM G 133 standards were used to establish the wear test parameters. Furthermore, constant load scratch tests were carried out with 50, 100, 150 and 200 N by the CSM Revetest-RST instrument. The test length was 5 mm. The wear depth and wear area after the ball-on-disk test were characterized by tactile measurements with the Hommel-Etamic T8000. The wear volume was determined using the 3D profilometer MikroCas (LMI, Teltow, Germany). Using a CSM instrument, the wear

depth after the scratch tests was detected. The wear tracks after the reciprocating wear tests were evaluated by the 3D profilometer MikroCas to record the wear depth and wear volume. SEM (BSD) was utilized to evaluate the wear tracks from the ball-on-disk and reciprocating tests.

**Table 2.** Wear test parameters.

| Ball-On-Disk Test |   | Reciprocating Wear Test |  | Scratch Test |                        |
|-------------------|---|-------------------------|--|--------------|------------------------|
| Force             | 20 N                                    | Force                   | 26 N                                     | Force        | Progressive 1–200 N    |
| Radius            | 5 mm                                    | Frequency               | 40 Hz                                    | Speed        | 2.5 mm/min             |
| Speed             | 96 RPM                                  | Time                    | 900 s                                    | Length       | 5 mm                   |
| Cycles            | 15,916                                  | Amplitude               | 0.5 mm                                   | Tip          | Truncated diamond cone |
| Counter body      | Al <sub>2</sub> O <sub>3</sub> (ø 6 mm) | Counter body            | Al <sub>2</sub> O <sub>3</sub> (ø 10 mm) | Radius       | 200 µm                 |

### 3. Results and Discussion

#### 3.1. Microstructure and Phase Formation

The microstructures of the SPS and LMD EHEA Al<sub>0.3</sub>CoCrFeNiNb<sub>0.5</sub> were characterized by SEM with a BSE detector. Images of the untreated and heat-treated SPS bulk material are shown in Figure 1.

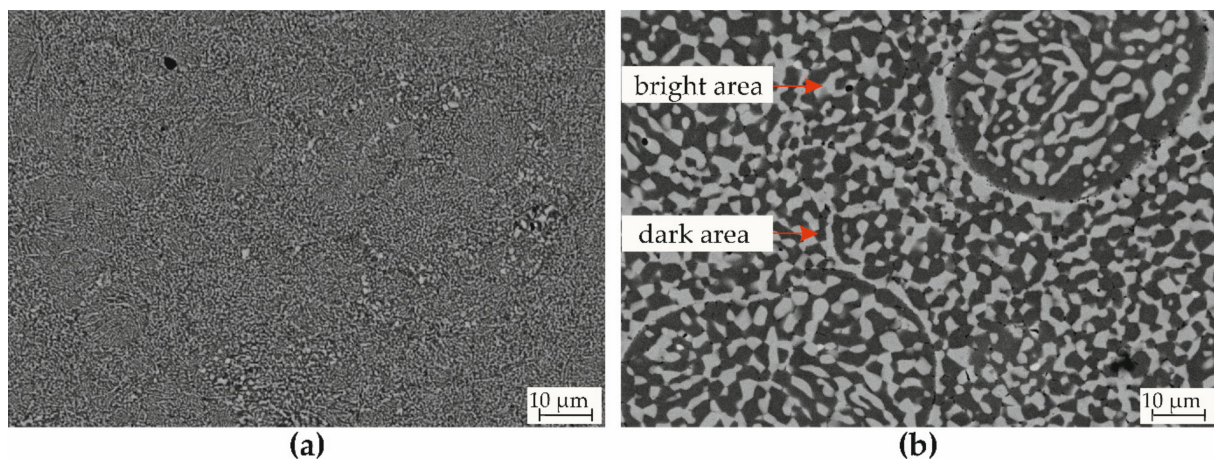


**Figure 1.** Microstructures (SEM, BSD) of the Al<sub>0.3</sub>CoCrFeNiNb<sub>0.5</sub> SPS bulk material: (a) untreated and (b) heat-treated. The contrast in the BSD images suggests the presence of at least two different phases. The untreated SPS bulk material exhibits a fine lamellar structure. Due to the heat treatment, the microstructure coarsened.

The SPS bulk material showed a few pores. A porosity of less than 1% was detected for both states. Both the untreated and heat-treated SPS bulk material exhibited a heterogeneous microstructure. The contrast in the BSD images suggests the presence of at least two phases with different compositions (dark and bright contrast). The dependence of the gray values on the atomic number suggests that the bright-appearing phase is rich in higher atomic number elements such as Nb. The opposite applies to the dark phases. A fine lamellar structure in the untreated condition was detected (Figure 1a). Coarser structures developed between the fine lamellae, especially at the particle boundaries. Different lamellar orientations were observed for the individual particles. During SPS processing, the particles are not remelted. Instead, recrystallization processes occur under high temperatures below the melting temperature and high pressures. Therefore, the microstructure of the feedstock powder is preserved in its lamellar orientation. Consequently, a statistically oriented lamellar structure is formed in the SPS bulk material. The heat treating of the SPS bulk material for 12 h at 1100 °C led to a microstructure coarsening (Figure 1b). The particle boundaries were occasionally marked by pronounced diffusion zones. The differences in

the lamellar orientation between the powder particles indicate a coarsening of the initial powder structure.

The coatings were produced by LMD. The microstructures of the coatings in their untreated and heat-treated states are demonstrated in Figure 2.

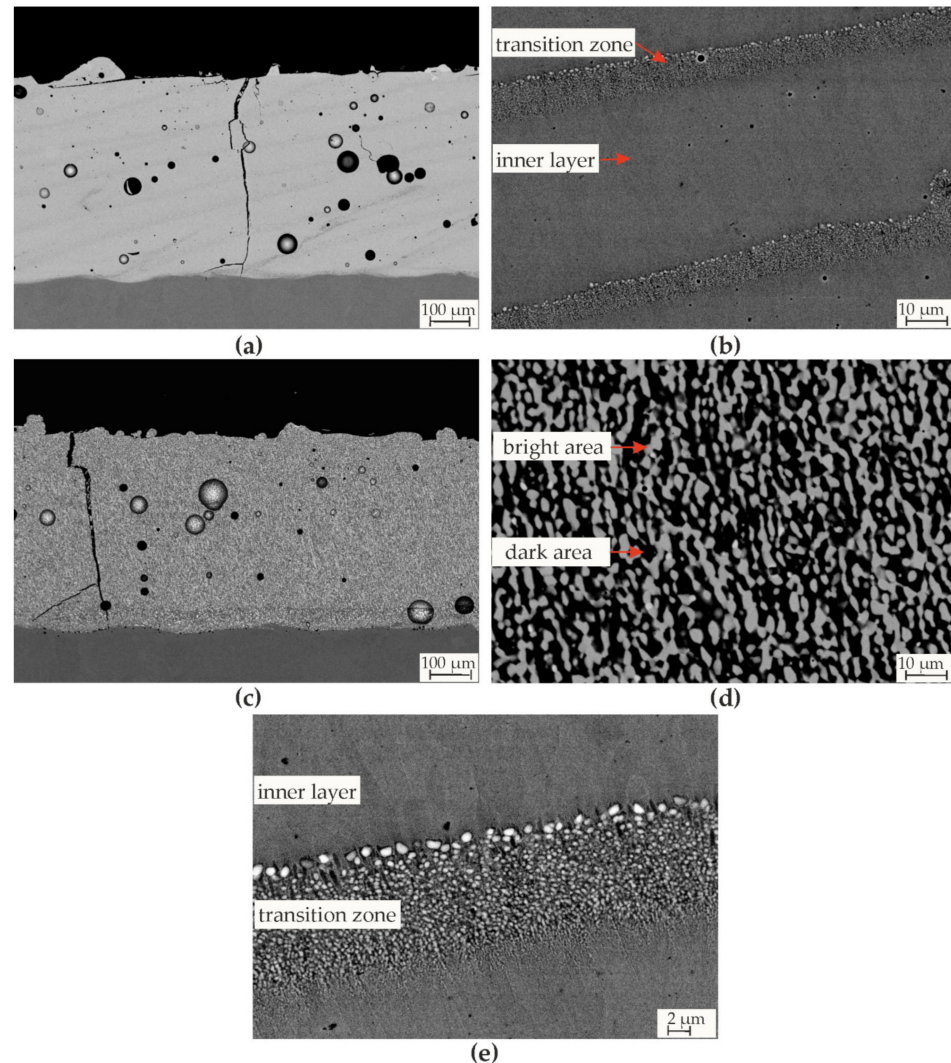


**Figure 2.** Microstructures (SEM, BSD) of the Al<sub>0.3</sub>CoCrFeNiNb<sub>0.5</sub> LMD coating: untreated (a) overview and (b), (e) detail; and heat-treated (c) overview and (d) detail. A directional solidification was observed in the untreated LMD coating. Due to the heat treatment, the microstructure coarsened and the distortion orientation of the lamellae was less pronounced.

Despite the good casting properties of eutectic alloys, the LMD coating exhibited cracks and pores. The porosity for the LMD coating was approx. 5%, with a coating thickness of approx. 500 μm. A closed porosity was observed, caused by the melting metallurgical production. The cracks could form because of different thermal expansion coefficients between the substrate and coating in combination with the fast cooling rates of LMD. A previous study on the powdered feedstock material illustrated the presence of pores within the particles [13]. These could have contributed to the pores within the coating. The pores could also have been created by breaking out large unmolded particles during preparation. Strips with a pronounced material contrast were detected, oriented at an angle of approx. 45° to the substrate. These represent the interface between the individual layers (transition zone), which were applied with a small offset of 300 μm. Due to the fusion of the layer surface, light-appearing precipitates were formed in the transition zone. The interface is

shown in the detailed images (Figure 2b,e). The LMD coating showed next to the transition zone, an ultrafine lamellar structure (Figure 2e), due to the high cooling rates during LMD. The detailed images (Figure 2e) show a longitudinally solidified microstructure. Directional solidification is caused by the high temperature gradient during cooling of the coating material. Similarly to the SPS bulk materials, a microstructure coarsening after heat treating was observed (Figure 2c,d). A clear material contrast can be seen in the overview image. At least two different phases were recognized.

The chemical composition of the cross sections was determined using an EDS detector. Table 3 shows the results of the EDS measurements. Due to the ultrafine lamellar structure in the untreated states, an area scan was performed instead of point measurements. The measured chemical composition was compared with the nominal composition. For the untreated SPS bulk material, no significant deviation from the nominal values was observed regarding the elements Co, Cr, Fe and Ni. Al and Nb showed larger deviations  $\geq 0.7$  at.%. For the heat-treated SPS bulk material, the chemical composition of the light and dark areas within the coarsened eutectic structure (Figure 1b) was recorded. The dark area showed a significantly lower Nb content, whereas the Ni, Fe, Cr and Al contents increased. The bright area was rich in Nb and Co and depleted in Al, Cr, Fe and Ni. Different studies on EHEAs with Nb have shown a similar result with respect to Nb- and Co-rich phases with an HCP lattice structure [30,33,34]. To clarify if different chemical compositions exist between the transition zone and the inner layer in the untreated LMD coating were analyzed, the differences between both areas compared to the nominal composition was  $\leq 1$  at.%. The bright area within the heat-treated LMD coating had a higher Nb content than those in the heat-treated SPS bulk material. As a result, the Cr, Fe, and Ni contents decreased. The chemical composition of the dark area in the heat-treated conditions was similar.

**Table 3.** The chemical composition of the untreated and heat-treated EHEA  $\text{Al}_{0.3}\text{CoCrFeNiNb}_{0.5}$  in at.% detected by EDS.

| Production Route | State        | Area            | Al  | Co   | Cr   | Fe   | Ni   | Nb   |
|------------------|--------------|-----------------|-----|------|------|------|------|------|
| Nominal          | -            | -               | 6.3 | 20.8 | 20.8 | 20.8 | 20.8 | 10.5 |
| SPS              | untreated    | -               | 5.6 | 20.7 | 20.8 | 20.9 | 20.5 | 11.5 |
|                  | heat-treated | dark area       | 7.2 | 20.2 | 22.9 | 22.7 | 23.8 | 3.2  |
|                  |              | bright area     | 3.5 | 20.6 | 19.2 | 19.1 | 17.0 | 20.6 |
| LMD              | untreated    | transition zone | 5.8 | 20.4 | 20.7 | 21.0 | 20.7 | 11.4 |
|                  |              | inner layer     | 6.4 | 20.4 | 20.8 | 20.5 | 20.7 | 11.2 |
|                  | heat-treated | dark area       | 7.4 | 20.3 | 22.8 | 22.4 | 24.1 | 3.0  |
|                  |              | bright area     | 3.4 | 20.4 | 18.1 | 18.6 | 16.0 | 23.5 |

The phase formation was investigated by XRD measurements. The diffraction patterns of the untreated and heat-treated bulk material and coating are shown in Figure 3. All measurements exhibited an FCC phase and HCP phase. The highest peak intensity was detected for the FCC phase. With regard to the EDS results, the darker phase of the microstructure could represent the detected FCC structure. Therefore, an FCC solid solution consisting primarily of Al, Co, Cr, Fe and Ni, which was depleted of Nb, was formed. Based on previous studies [33,34] and the EDS measurements, an Nb- and Co-rich HCP phase formed in this alloy system. Detailed examinations of the diffractograms showed a decrease in peak width after heat treatment for both systems. The width of the individual peaks is decisively influenced by the residual stress state and the defect density (Scherrer equation [35]). Both the SPS and LMD coatings showed a reduction of the peak width in the heat-treated state. This is due to diffusion and recrystallization processes. This effect was much more pronounced within the LMD coating since the sintering process reduces the disequilibrium state. A peak shift of the FCC phase to smaller angles and of the HCP phase to higher angles was observed for the untreated LMD coating in Figure 3 compared

to all other conditions. Therefore, the lattice spacing of the FCC phase increased and of the HCP phase, decreased. This shift could be attributed to the high cooling rates and consequently reduced diffusion processes during LMD. Accordingly, an FCC solid solution that was supersaturated was formed. Heat treating and sintering led to a peak shift of the FCC phase to higher angles and of the HCP phases to smaller angles. Diffusion and recrystallization could be responsible for this. A similar diffusion tendency of Nb was observed in the EHEA CoCrFeNiNb<sub>x</sub> [30].

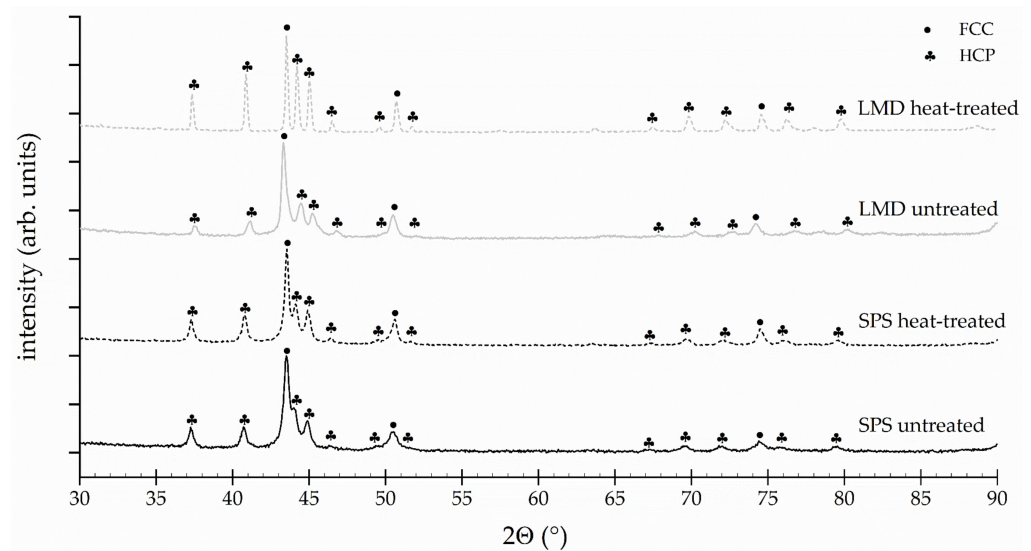


**Figure 3.** Diffractograms of Al<sub>0.3</sub>CoCrFeNiNb<sub>0.5</sub> untreated and heat-treated SPS bulk material and LMD coating. An FCC phase and HCP phase were detected for all conditions. A peak shift was observed for the untreated LMD coating. The high cooling rates during LMD could have caused the formation of an FCC supersaturated solid solution.

Table 4 shows the lattice parameters derived from the XRD measurements. A slight increase in the lattice parameter of 3.61 Å was detected for the untreated LMD coating. Lattice distortion due to the incorporation of elements with a larger atomic radius such as Nb could have been responsible for this. In the HCP phase of the untreated LMD coating, a decrease in the lattice parameter was detected. This could be attributed to a decrease in the proportions of atoms with a large atomic radius such as Nb. The lattice of the HCP phase was widened and the distortion of the FCC lattice was reduced by recrystallization and diffusion processes during sintering and heat treatment.

**Table 4.** Lattice parameters of the FCC and HCP phases determined by XRD for the bulk material and LMD coating of the EHEA Al<sub>0.3</sub>CoCrFeNiNb<sub>0.5</sub>.

| State            | Lattice Parameter |            |            |
|------------------|-------------------|------------|------------|
|                  | FCC               | HCP        |            |
| SPS untreated    | a = 3.60 Å        | a = 4.83 Å | c = 7.85 Å |
| SPS heat-treated | a = 3.60 Å        | a = 4.82 Å | c = 7.83 Å |
| LMD untreated    | a = 3.61 Å        | a = 4.79 Å | c = 7.77 Å |
| LMD heat-treated | a = 3.60 Å        | a = 4.85 Å | c = 7.80 Å |

### 3.2. Microhardness and Wear Behavior

The influence of the production route and heat treatment on the resulting surface hardness was recorded for the EHEA Al<sub>0.3</sub>CoCrFeNiNb<sub>0.5</sub> (Figure 4).

Both production routes showed a heat treatment-induced decrease in hardness. Microstructural coarsening could be the reason. Due to this, the number of phase boundaries decreases, and consequently, dislocation movement is less inhibited. The highest average

hardness was achieved for the untreated LMD coating with 715 HV0.5. The high hardness resulted from rapid cooling from the melt. Therefore, an ultrafine lamellar structure could develop in combination with a solid solution strengthening. The untreated SPS bulk material exhibited a significantly lower hardness of 572 HV0.5. The eutectic structure was much more pronounced compared to the untreated LMD coating. This was associated with a decrease in the number of phase boundaries, and consequently, the hardness. In the heat-treated state, no significant difference between the SPS bulk material and the LMD coating in hardness can be seen. Consequently, a similar coarsened eutectic structure was produced regardless of the lamellar size before the heat treatment. The as-cast condition of the EHEA  $\text{Al}_{0.3}\text{CoCrFeNiNb}_{0.5}$  had a hardness of approx. 650 HV0.5 [13]. This reduced hardness compared to the untreated LMD coating can be attributed to the larger lamellae and lamellar spacing. Löbel et al. also observed a coarsening of the microstructure and an associated decrease in hardness for the HEA  $\text{AlCrFeCoNi}$  [36].

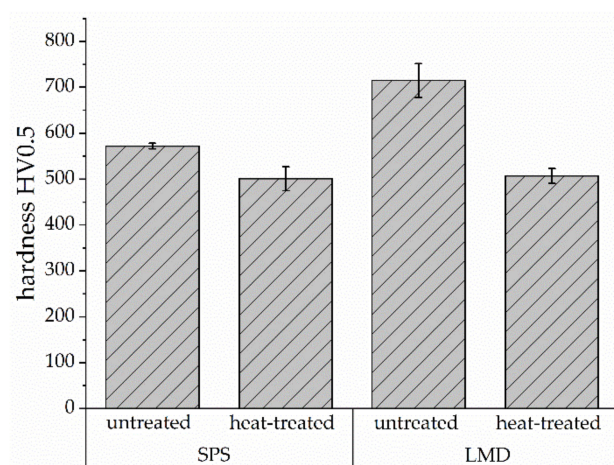


**Figure 4.** Microhardness of the untreated and heat-treated SPS bulk material and laser metal deposited (LMD) sample  $\text{Al}_{0.3}\text{CoCrFeNiNb}_{0.5}$ . The highest hardness was detected for the untreated LMD coating. By heat-treating, a hardness decrease was detected.

The correlation between the local microstructure domain size and texture and the wear resistance was investigated. Ball-on-disk, reciprocating and scratch tests were conducted to determine the resistance to different wear conditions. The results of the ball-on-disk test are shown in Figure 5. The untreated LMD exhibited the highest sliding wear resistance, possibly due to the ultrafine lamellar structure and solid solution strengthening. However, the untreated SPS sample was found to have the highest wear depth and wear area compared to all other conditions. The statistical orientation of the microstructure could be the reason for the reduced wear resistance. In contrast, the LMD coating had a structure vertically oriented to the transition zone. The constant rectified phase transitions could reduce the shear of the phase fractions. Independent of the production route, the heat-treated SPS bulk material and LMD coating showed similar wear values. The heat treatment led to an improvement in wear resistance for the SPS bulk material due to homogenization of the microstructure. In particular, the periodic orientation of the microstructure compared to the untreated SPS bulk material improved the wear resistance. The microstructure coarsening led to a decrease in wear resistance compared to the untreated LMD coating. This could be due to the lower hardness and differences in lamellar orientation. Based on a previous study [13] on cast specimens of EHEA  $\text{Al}_{0.3}\text{CoCrFeNiNb}_{0.5}$ , a similar wear depth and volume were determined as for the untreated SPS bulk material. A similar lamellar size and phase composition could account for these.

Detailed investigations of the wear tracks after the ball-on-disk test were carried out to detect the wear mechanism. SEM images (BSD) of the worn surface are shown in Figure 6. The untreated SPS bulk material (Figure 6a) showed a strong material contrast. The darker areas indicate a higher concentration of elements with a low atomic number.

EDS measurements of the darker area showed a high amount of oxygen. Hence, oxides were formed. The bright area can be attributed to the EHEA. Flakes and grooves were observed on the oxide layer surface. The two-dimensional oxides were formed by the wear impact. This caused a rapid breakout of oxides, leading to deeper wear tracks. A dislodged particle was also identifiable. The wear track of the untreated LMD coating (Figure 6c) showed primarily grooves and exposed pores. Accordingly, the dominant wear mechanism was abrasion. The heat-treated SPS bulk material (Figure 6b) and LMD coating (Figure 6d) exhibited pronounced flakes on the whole wear surface. Individual grooves and oxidation were still evident, but surface deformation and surface fatigue were dominant. Furthermore, two-dimensional oxides were integrated into the surface.

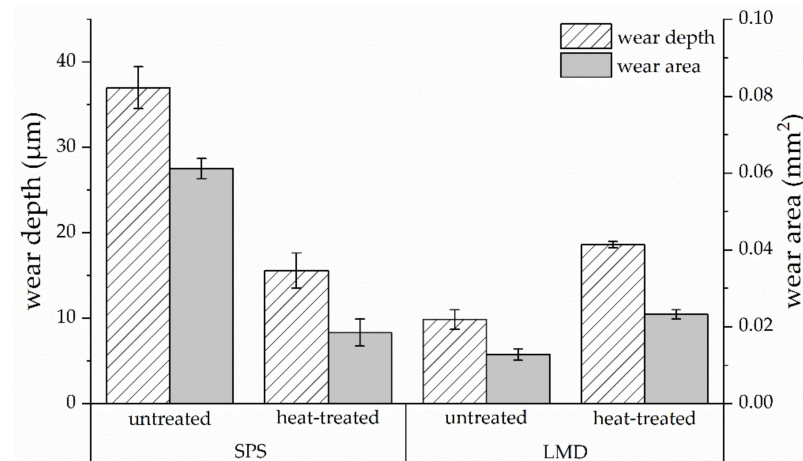


**Figure 5.** Ball-on-disk test of the untreated and heat-treated SPS bulk material and LMD coating of  $\text{Al}_{0.3}\text{CoCrFeNiNb}_{0.5}$ . The untreated LMD coating showed the highest sliding wear resistance. By heat treating the SPS bulk material, improvement in wear resistance was realized.

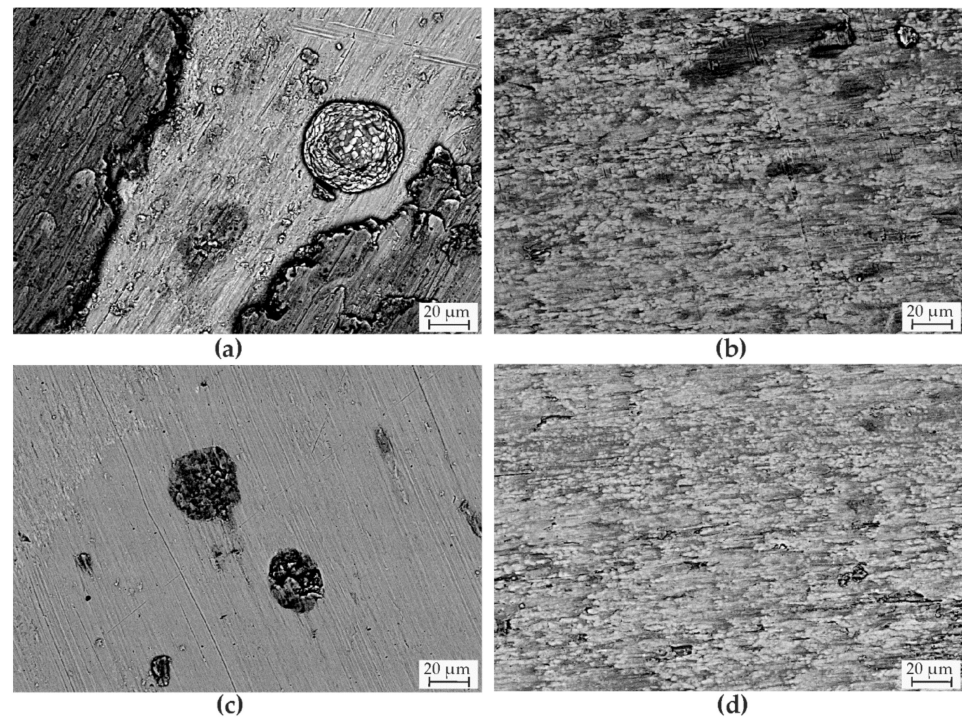


**Figure 6.** Surfaces (SEM, BSD) of the EHEA  $\text{Al}_{0.3}\text{CoCrFeNiNb}_{0.5}$  after ball-on-disk testing of (a) untreated and (b) heat-treated SPS bulk material as well as (c) untreated and (d) heat-treated LMD coating. Plastic deformation can be observed for all conditions.

The oscillating wear resistance of the SPS bulk material and LMD coating was investigated by reciprocating wear tests. The results are shown in Figure 7. The untreated SPS bulk material exhibited the highest wear resistance.

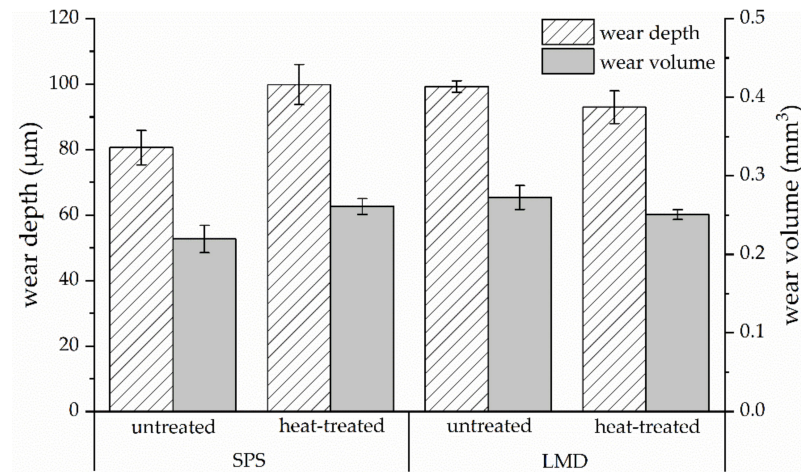


**Figure 7.** Reciprocating wear test of the untreated and heat-treated SPS bulk material and LMD coating of  $\text{Al}_{0.3}\text{CoCrFeNiNb}_{0.5}$ . The untreated SPS bulk material exhibited the highest wear resistance. By heat treatment, the wear resistance increased for the LMD coating and decreased for the SPS bulk material.

Similar wear depths were recorded as for the  $\text{Al}_{0.3}\text{CoCrFeNiNb}_{0.5}$  casting [13] investigated in a previous study. On the other hand, the wear volume of the casting was lower. Defects such as pores could be the reason. However, a change in the phase composition of the cast specimen compared to the SPS bulk material due to the melting metallurgical casting production is also possible. Compared to the untreated SPS bulk material, the wear depth and wear volume increased for the untreated LMD coating, possibly due to the brittle behavior of the LMD coating. The untreated and heat-treated LMD coatings as well as the heat-treated SPS bulk material exhibited a similar wear resistance. Hence, the preferred orientation of the phases under oscillating wear conditions had no significant influence.

Figure 8 shows the SEM images (BSD) of the worn surface after reciprocating wear tests. A clear material contrast can be seen for all conditions.

By EDS, increased oxygen content could be qualitatively detected. All conditions exhibited distinct cracks and flakes in the oxidized layer. This indicates the continuous formation and removal of oxides. Plastic deformation along the wear direction was detected for the heat-treated conditions. The SEM images show a pronounced bonding of the oxides in the matrix for the untreated SPS bulk material. It seems to be that the oxides were insufficiently bound to the surface of the untreated LMD coatings and the heat-treated states. The harder and thus more brittle microstructure of the LMD coatings could prevent firm bonding of the oxides. The coarsened microstructures after heat treatment showed significant differences in chemical composition between the phases. Therefore, the formation of stable oxides could be prevented.

Figure 9 summarizes the calculated wear rates after the ball-on-disk and reciprocating wear tests. The comparison of the different wear conditions showed a better resistance to sliding wear than to oscillating wear for the heat-treated SPS bulk material and the LMD coatings. Only the untreated SPS material showed a higher wear rate under sliding wear than under oscillating wear conditions.

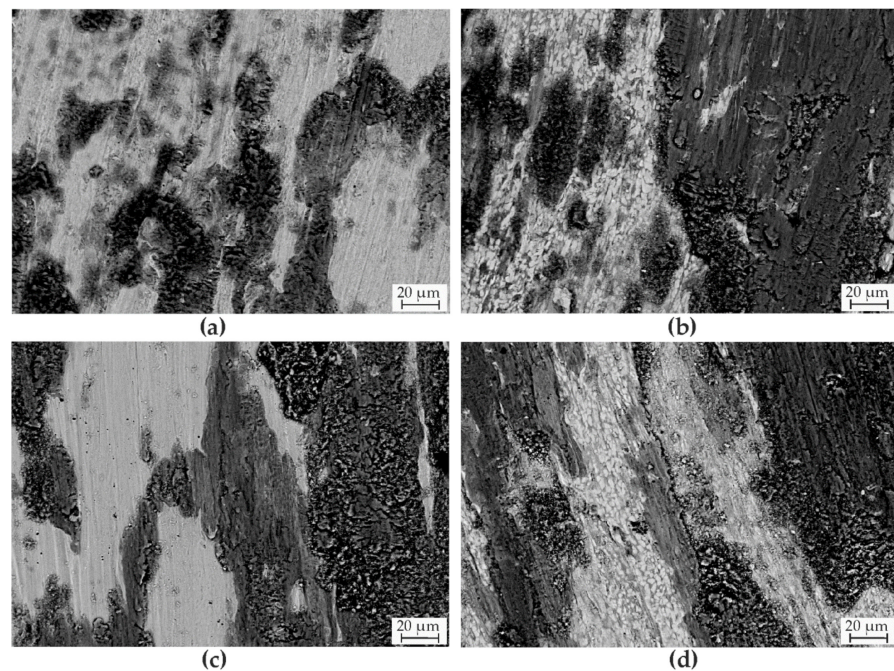


**Figure 8.** Surfaces (SEM, BSD) of the EHEA  $\text{Al}_{0.3}\text{CoCrFeNiNb}_{0.5}$  after ball-on-disk testing of (a) untreated and (b) heat-treated SPS bulk material as well as (c) untreated and (d) heat-treated LMD coating. Oxidational wear was identified for all conditions. Grooves were detected in the untreated conditions. Due to heat treatment, the wear tracks showed plastic deformation.

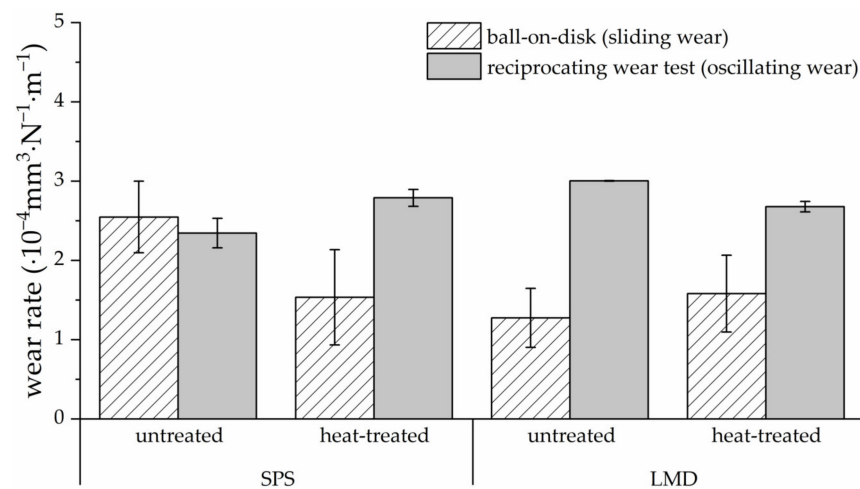


**Figure 9.** Ball-on-disk (sliding wear conditions) and reciprocating (oscillating wear conditions) wear rates  $K$  for the untreated and heat-treated SPS bulk material as well as LMD coating. The untreated SPS bulk material showed a higher resistance to sliding wear. All other conditions showed the contrary.

Scratch tests were conducted at a progressive load between 1–200 N. The results of are shown in Figure 10. The scratch test curve characteristics allow for a statement about the surface/coating quality. For all conditions, the residual depth increased almost constantly with an increasing load. The straight line gradient of the SPS materials suggests a high surface quality. The highest wear depth for the SPS bulk materials was achieved at a maximum load. The LMD coatings exhibited distinct peaks associated with defects such as pores and cracks. These microstructural defects have already been demonstrated by the SEM images (Figure 2). Consequently, the maximum wear depth was often detected at loads lower than 200 N.

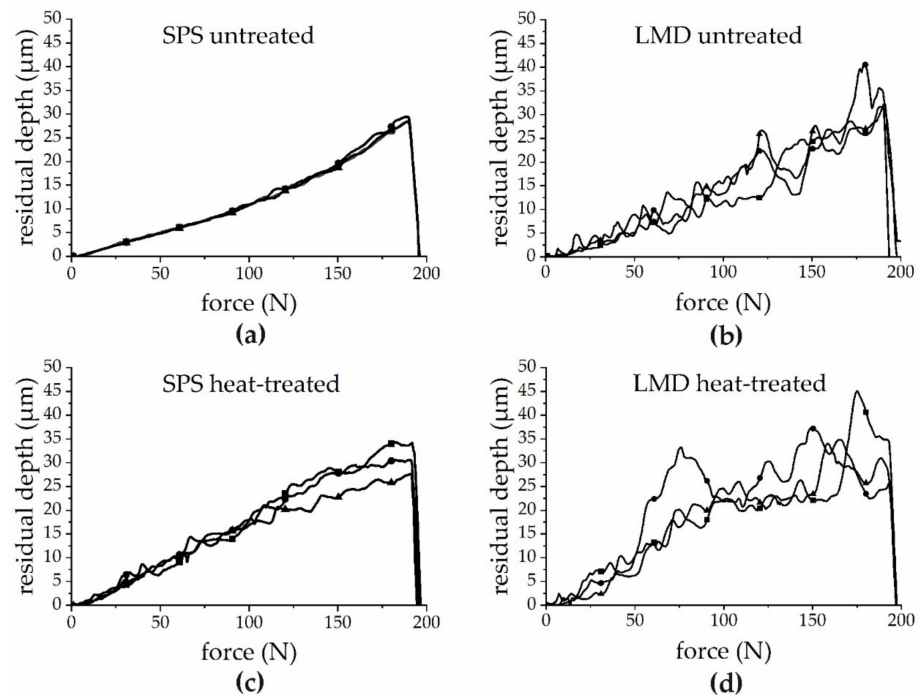


**Figure 10.** Progressive load scratch testing of (a) untreated and (c) heat-treated SPS bulk material as well as (b) untreated and (d) heat-treated LMD coating. The straight line gradient of the SPS bulk materials suggests a high surface quality with a low number of pores and cracks.

To determine the abrasive wear properties of the EHEA  $Al_{0.3}CoCrFeNiNb_{0.5}$ , scratch tests were carried out under the constant loads 50, 100, 150 and 200 N (Figure 11). Therefore, the influence of defects such as pores and cracks was minimized.

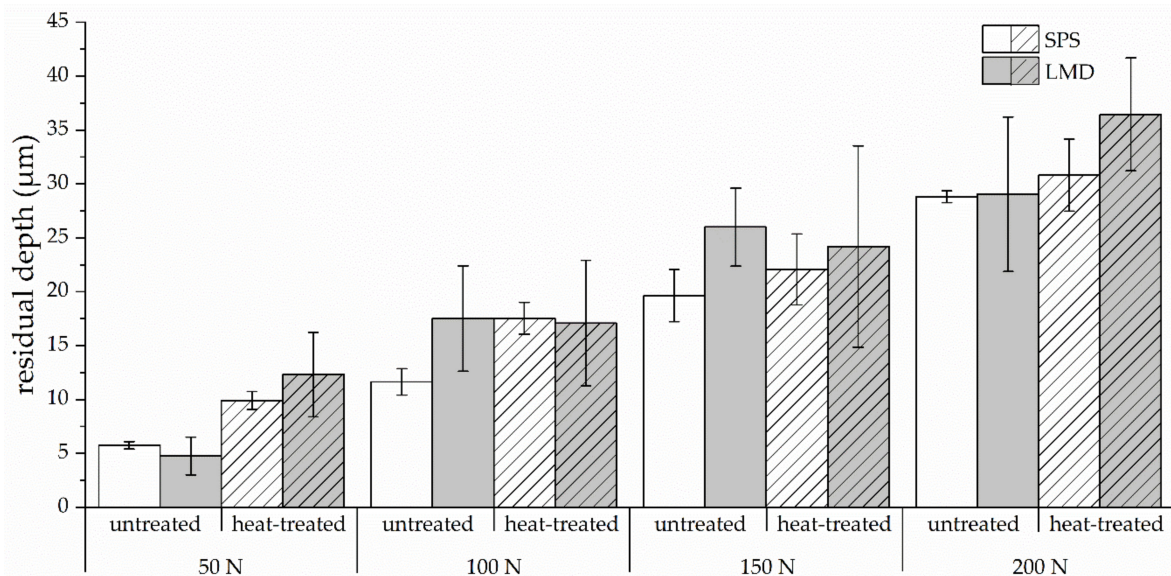


**Figure 11.** Constant load scratch testing of the untreated and heat-treated SPS bulk material and LMD coating of  $Al_{0.3}CoCrFeNiNb_{0.5}$ . Under various constant loads, the untreated SPS bulk material exhibited high abrasive wear resistance.

The average wear depth significantly increased for the heat-treated conditions at a load of 50 N. The coarsening of the microstructure in connection with the decrease in phase boundaries could be the reason. By increasing the test load to 100 N, the untreated SPS bulk material showed the highest abrasive wear resistance probably due to the low proportion

of structural effects in combination with a fine lamellar structure. The untreated LMD coating exhibited the highest average wear depth at 150 N. Brittle behavior and structural defects could be the reason. At the maximum load of 200 N, the influence of heat treatment was almost undetectable for the untreated and heat-treated SPS bulk material. The heat-treated LMD coating exhibited the highest average wear depth at a maximum load. This could be due to the interaction between the coarsened microstructure and the structural defects. An influence of the lamellar orientation on wear resistance under abrasive wear was not observed.

#### 4. Summary and Conclusions

In this study, the influence of the production conditions on the functional properties of EHEA  $\text{Al}_{0.3}\text{CoCrFeNiNb}_{0.5}$  due to size and texture modifications of the local microstructural domain was investigated. Therefore, the inert gas atomized powder was further processed to bulk materials by SPS as well as to coatings by LMD. A heat treatment at 1100 °C for 12 h was performed. Microhardness measurements and different wear tests were carried out in order to determine the influence of the microstructure characteristics caused by the production route. For the EHEA  $\text{Al}_{0.3}\text{CoCrFeNiNb}_{0.5}$ , the following findings can be drawn:

- Higher cooling rates in the LMD process compared to SPS led to an ultrafine eutectic structure with solid solution strengthening. Hence, the highest microhardness was detected. Furthermore, directional solidification vertical to the transition zone was determined for the LMD coating. The SPS bulk materials were shown within each particle preferential direction.
- The directionally solidified ultrafine lamellar structure of the LMD coating improved the resistance to sliding wear. This could be due to the reduced shear of the directional phase fractions. Meanwhile, the statistically distributed orientation of the lamellar structure in the SPS bulk material caused a higher reciprocating wear resistance. Pronounced bonding of the oxides in the SPS bulk material could be the reason.
- The lamellar size instead of the preferred orientation dominated the functional properties of the heat-treated LMD coating and SPS bulk material. Hence, the heat-treated specimens with similar lamellar characteristics exhibited a comparable property profile regardless of the production route.
- An improvement in the sliding wear resistance was realized by heat-treating the SPS bulk material. The periodic orientation of the microstructure compared to the statistically distributed lamellae in the untreated SPS bulk material could be responsible.

The present study demonstrates a microstructural modification of the EHEA  $\text{Al}_{0.3}\text{CoCrFeNiNb}_{0.5}$  depending on the production route and heat treatment. Therefore, the hardness and wear resistance were decisively influenced. Further tests with different heat treatment parameters have to be conducted to understand the microstructural stability and eutectic reaction. Furthermore, by using other production routes, the influence of the cooling rate and processing conditions on the microstructure and properties should be investigated. Based on these findings, application areas and production routes can be further refined.

**Author Contributions:** Conceptualization, B.P.; methodology, B.P., T.L. (Thomas Lindner) and T.U.; validation, T.L. (Thomas Lindner), T.U., J.E.T.C. and H.S.; investigation, B.P., T.U., J.E.T.C. and H.S.; writing—original draft preparation, B.P. and T.L. (Thomas Lindner); writing—review and editing, T.L. (Thomas Lindner), G.W., T.S. and T.L. (Thomas Lampke); supervision, T.L. (Thomas Lindner); project administration, T.L. (Thomas Lindner) and T.L. (Thomas Lampke); funding acquisition, T.L. (Thomas Lindner). All authors have read and agreed to the published version of the manuscript.

**Funding:** This study was funded via Sächsische Aufbaubank–Förderbank/SAB-100382175, by the European Social Fund (ESF) and the Free State of Saxony. The publication of this article was funded by Chemnitz University of Technology and by the Deutsche Forschungsgemeinschaft (DFG, German Research Foundation)—491193532.



Diese Maßnahme wird mitfinanziert durch Steuermittel auf der Grundlage des vom Sächsischen Landtag beschlossenen Haushaltes.

**Institutional Review Board Statement:** Not applicable.

**Informed Consent Statement:** Not applicable.

**Data Availability Statement:** Not applicable.

**Acknowledgments:** The support from Steffen Clauß (Institute of Materials Science and Engineering) is gratefully acknowledged.

**Conflicts of Interest:** The authors declare no conflict of interest.

## References

- Gao, M.C.; Yeh, J.-W.; Liaw, P.K.; Zhang, Y. *High-Entropy Alloys: Fundamentals and Applications*; Softcover Reprint of the Original 1st Edition 2016; Springer International Publishing: Cham, Switzerland, 2018; ISBN 978-3-319-80057-8.
- Meghwal, A.; Anupam, A.; Murty, B.S.; Berndt, C.C.; Kottada, R.S.; Ang, A.S.M. Thermal Spray High-Entropy Alloy Coatings: A Review. *J. Therm. Spray Technol.* **2020**, *29*, 857–893. [[CrossRef](#)]
- Lu, Y.; Dong, Y.; Jiang, H.; Wang, Z.; Cao, Z.; Guo, S.; Wang, T.; Li, T.; Liaw, P.K. Promising Properties and Future Trend of Eutectic High Entropy Alloys. *Scr. Mater.* **2020**, *187*, 202–209. [[CrossRef](#)]
- Moravcik, I.; Cizek, J.; Gavendova, P.; Sheikh, S.; Guo, S.; Dlouhy, I. Effect of Heat Treatment on Microstructure and Mechanical Properties of Spark Plasma Sintered AlCoCrFeNiTi0.5 High Entropy Alloy. *Mater. Lett.* **2016**, *174*, 53–56. [[CrossRef](#)]
- Singh, S.; Wanderka, N.; Murty, B.S.; Glatzel, U.; Banhart, J. Decomposition in Multi-Component AlCoCrCuFeNi High-Entropy Alloy. *Acta Mater.* **2011**, *59*, 182–190. [[CrossRef](#)]
- Yeh, J.-W.; Chen, S.-K.; Lin, S.-J.; Gan, J.-Y.; Chin, T.-S.; Shun, T.-T.; Tsau, C.-H.; Chang, S.-Y. Nanostructured High-Entropy Alloys with Multiple Principal Elements: Novel Alloy Design Concepts and Outcomes. *Adv. Eng. Mater.* **2004**, *6*, 299–303. [[CrossRef](#)]
- Zhang, Y.; Zuo, T.T.; Tang, Z.; Gao, M.C.; Dahmen, K.A.; Liaw, P.K.; Lu, Z.P. Microstructures and Properties of High-Entropy Alloys. *Prog. Mater. Sci.* **2014**, *61*, 1–93. [[CrossRef](#)]
- Lu, Y.; Dong, Y.; Guo, S.; Jiang, L.; Kang, H.; Wang, T.; Wen, B.; Wang, Z.; Jie, J.; Cao, Z.; et al. A Promising New Class of High-Temperature Alloys: Eutectic High-Entropy Alloys. *Sci. Rep.* **2015**, *4*, 6200. [[CrossRef](#)]
- Jiang, H.; Qiao, D.; Lu, Y.; Ren, Z.; Cao, Z.; Wang, T.; Li, T. Direct Solidification of Bulk Ultrafine-Microstructure Eutectic High-Entropy Alloys with Outstanding Thermal Stability. *Scr. Mater.* **2019**, *165*, 145–149. [[CrossRef](#)]
- Guo, Y.; Liu, L.; Zhang, Y.; Qi, J.; Wang, B.; Zhao, Z.; Shang, J.; Xiang, J. A Superfine Eutectic Microstructure and the Mechanical Properties of CoCrFeNiMo<sub>x</sub> High-Entropy Alloys. *J. Mater. Res.* **2018**, *33*, 3258–3265. [[CrossRef](#)]
- Jiang, H.; Zhang, H.; Huang, T.; Lu, Y.; Wang, T.; Li, T. Microstructures and Mechanical Properties of Co<sub>2</sub>MoxNi<sub>2</sub>VW<sub>x</sub> Eutectic High Entropy Alloys. *Mater. Des.* **2016**, *109*, 539–546. [[CrossRef](#)]
- Jiao, W.; Jiang, H.; Qiao, D.; He, J.; Zhao, H.; Lu, Y.; Li, T. Effects of Mo on Microstructure and Mechanical Properties of Fe<sub>2</sub>Ni<sub>2</sub>CrMox Eutectic High Entropy Alloys. *Mater. Chem. Phys.* **2021**, *260*, 124175. [[CrossRef](#)]
- Preuß, B.; Lindner, T.; Uhlig, T.; Wagner, G.; Lampke, T. Niobium and Molybdenum as Alloying Constituents in Al<sub>0.3</sub>CoCrFeNi to Develop Eutectic High-Entropy Alloys for HVOF Spraying. *J. Therm. Spray Technol.* **2022**, 1–10. [[CrossRef](#)]
- Wu, Z.; Bei, H.; Otto, F.; Pharr, G.M.; George, E.P. Recovery, Recrystallization, Grain Growth and Phase Stability of a Family of FCC-Structured Multi-Component Equiatomic Solid Solution Alloys. *Intermetallics* **2014**, *46*, 131–140. [[CrossRef](#)]
- Wang, W.-R.; Wang, W.-L.; Yeh, J.-W. Phases, Microstructure and Mechanical Properties of AlxCoCrFeNi High-Entropy Alloys at Elevated Temperatures. *J. Alloys Compd.* **2014**, *589*, 143–152. [[CrossRef](#)]
- Zhang, A.; Han, J.; Meng, J.; Su, B.; Li, P. Rapid Preparation of AlCoCrFeNi High Entropy Alloy by Spark Plasma Sintering from Elemental Powder Mixture. *Mater. Lett.* **2016**, *181*, 82–85. [[CrossRef](#)]
- Ji, W.; Wang, W.; Wang, H.; Zhang, J.; Wang, Y.; Zhang, F.; Fu, Z. Alloying Behavior and Novel Properties of CoCrFeNiMn High-Entropy Alloy Fabricated by Mechanical Alloying and Spark Plasma Sintering. *Intermetallics* **2015**, *56*, 24–27. [[CrossRef](#)]
- Moravcik, I.; Cizek, J.; Zapletal, J.; Kovacova, Z.; Vesely, J.; Minarik, P.; Kitzmantel, M.; Neubauer, E.; Dlouhy, I. Microstructure and Mechanical Properties of Ni<sub>1.5</sub>Co<sub>1.5</sub>CrFeTi<sub>0.5</sub> High Entropy Alloy Fabricated by Mechanical Alloying and Spark Plasma Sintering. *Mater. Des.* **2017**, *119*, 141–150. [[CrossRef](#)]
- Riva, S.; Brown, S.G.R.; Lavery, N.P.; Tudball, A.; Yusenkov, K.V. Spark Plasma Sintering of High Entropy Alloys. In *Spark Plasma Sintering of Materials*; Cavaliere, P., Ed.; Springer International Publishing: Cham, Switzerland, 2019; pp. 517–538, ISBN 978-3-030-05326-0.

20. Sriharitha, R.; Murty, B.S.; Kottada, R.S. Alloying, Thermal Stability and Strengthening in Spark Plasma Sintered Al<sub>x</sub>CoCrFeNi High Entropy Alloys. *J. Alloys Compd.* **2014**, *583*, 419–426. [[CrossRef](#)]
21. Cieslak, J.; Tobola, J.; Berent, K.; Marciszko, M. Phase Composition of Al<sub>x</sub>FeNiCrCo High Entropy Alloys Prepared by Sintering and Arc-Melting Methods. *J. Alloys Compd.* **2018**, *740*, 264–272. [[CrossRef](#)]
22. Pan, W.; Fu, P.; Li, Z.; Chen, H.; Tang, Q.; Dai, P.; Liu, C.; Lin, L. Microstructure and Mechanical Properties of AlCoCrFeNi<sub>2.1</sub> Eutectic High-Entropy Alloy Synthesized by Spark Plasma Sintering of Gas-Atomized Powder. *Intermetallics* **2022**, *144*, 107523. [[CrossRef](#)]
23. Shamsaei, N.; Yadollahi, A.; Bian, L.; Thompson, S.M. An Overview of Direct Laser Deposition for Additive Manufacturing; Part II: Mechanical Behavior, Process Parameter Optimization and Control. *Addit. Manuf.* **2015**, *8*, 12–35. [[CrossRef](#)]
24. Zhang, Y.; Koch, C.C.; Ma, S.G.; Zhang, H.; Pan, Y. Fabrication Routes. In *High-Entropy Alloys*; Gao, M.C., Yeh, J.-W., Liaw, P.K., Zhang, Y., Eds.; Springer International Publishing: Cham, Switzerland, 2016; pp. 151–179. ISBN 978-3-319-27011-1.
25. Lindner, T.; Liborius, H.; Töberling, G.; Vogt, S.; Preuß, B.; Rymer, L.-M.; Schubert, A.; Lampke, T. High-Speed Laser Metal Deposition of CrFeCoNi and AlCrFeCoNi HEA Coatings with Narrow Intermixing Zone and Their Machining by Turning and Diamond Smoothing. *Coatings* **2022**, *12*, 879. [[CrossRef](#)]
26. Qiu, X.-W.; Liu, C.-G. Microstructure and Properties of Al<sub>2</sub>CrFeCoCuTiNi High-Entropy Alloys Prepared by Laser Cladding. *J. Alloys Compd.* **2013**, *553*, 216–220. [[CrossRef](#)]
27. Wen, X.; Cui, X.; Jin, G.; Liu, Y.; Zhang, Y.; Fang, Y. In-Situ Synthesis of Nano-Lamellar Ni<sub>1.5</sub>CrCoFe<sub>0.5</sub>Mo<sub>0.1</sub>Nb<sub>x</sub> Eutectic High-Entropy Alloy Coatings by Laser Cladding: Alloy Design and Microstructure Evolution. *Surf. Coat. Technol.* **2021**, *405*, 126728. [[CrossRef](#)]
28. Baker, I.; Wu, M.; Wang, Z. Eutectic/Eutectoid Multi-Principle Component Alloys: A Review. *Mater. Charact.* **2019**, *147*, 545–557. [[CrossRef](#)]
29. Huang, L.; Sun, Y.; Chen, N.; Luan, H.; Le, G.; Liu, X.; Ji, Y.; Lu, Y.; Liaw, P.K.; Yang, X.; et al. Simultaneously Enhanced Strength-Ductility of AlCoCrFeNi<sub>2.1</sub> Eutectic High-Entropy Alloy via Additive Manufacturing. *Mater. Sci. Eng. A* **2022**, *830*, 142327. [[CrossRef](#)]
30. Cao, X.; Wu, C.; Liu, Y.; Peng, H.; Su, X. Eutectic Reaction and Microstructure Stability in CoCrFeNiNb<sub>x</sub> High-Entropy Alloys. *Metals* **2022**, *12*, 756. [[CrossRef](#)]
31. Jiang, L.; Lu, Y.; Wu, W.; Cao, Z.; Li, T. Microstructure and Mechanical Properties of a CoFeNi<sub>2</sub>V<sub>0.5</sub>Nb<sub>0.75</sub> Eutectic High Entropy Alloy in As-Cast and Heat-Treated Conditions. *J. Mater. Sci. Technol.* **2016**, *32*, 245–250. [[CrossRef](#)]
32. John, R.; Karati, A.; Joseph, J.; Fabijanic, D.; Murty, B.S. Microstructure and Mechanical Properties of a High Entropy Alloy with a Eutectic Composition (AlCoCrFeNi<sub>2.1</sub>) Synthesized by Mechanical Alloying and Spark Plasma Sintering. *J. Alloys Compd.* **2020**, *835*, 155424. [[CrossRef](#)]
33. Jiang, H.; Jiang, L.; Qiao, D.; Lu, Y.; Wang, T.; Cao, Z.; Li, T. Effect of Niobium on Microstructure and Properties of the CoCrFeNb<sub>x</sub> Ni High Entropy Alloys. *J. Mater. Sci. Technol.* **2017**, *33*, 712–717. [[CrossRef](#)]
34. Liu, W.H.; He, J.Y.; Huang, H.L.; Wang, H.; Lu, Z.P.; Liu, C.T. Effects of Nb Additions on the Microstructure and Mechanical Property of CoCrFeNi High-Entropy Alloys. *Intermetallics* **2015**, *60*, 1–8. [[CrossRef](#)]
35. Scherrer, P. Bestimmung der inneren Struktur und der Größe von Kolloidteilchen mittels Röntgenstrahlen. In *Kolloidchemie Ein Lehrbuch*; Springer: Berlin/Heidelberg, Germany, 1912; pp. 387–409. ISBN 978-3-662-33517-8.
36. Löbel, M.; Lindner, T.; Clauß, S.; Pippig, R.; Dietrich, D.; Lampke, T. Microstructure and Wear Behavior of the High-Velocity-Oxygen-Fuel Sprayed and Spark Plasma Sintered High-Entropy Alloy AlCrFeCoNi. *Adv. Eng. Mater.* **2021**, *23*, 2001253. [[CrossRef](#)]

**Disclaimer/Publisher’s Note:** The statements, opinions and data contained in all publications are solely those of the individual author(s) and contributor(s) and not of MDPI and/or the editor(s). MDPI and/or the editor(s) disclaim responsibility for any injury to people or property resulting from any ideas, methods, instructions or products referred to in the content.